

RSC Advances



This is an *Accepted Manuscript*, which has been through the Royal Society of Chemistry peer review process and has been accepted for publication.

Accepted Manuscripts are published online shortly after acceptance, before technical editing, formatting and proof reading. Using this free service, authors can make their results available to the community, in citable form, before we publish the edited article. This *Accepted Manuscript* will be replaced by the edited, formatted and paginated article as soon as this is available.

You can find more information about *Accepted Manuscripts* in the [Information for Authors](#).

Please note that technical editing may introduce minor changes to the text and/or graphics, which may alter content. The journal's standard [Terms & Conditions](#) and the [Ethical guidelines](#) still apply. In no event shall the Royal Society of Chemistry be held responsible for any errors or omissions in this *Accepted Manuscript* or any consequences arising from the use of any information it contains.

ARTICLE

Polyimide/Graphene Composite Foam Sheets with Ultrahigh Thermostability for Electromagnetic Interference Shielding

Cite this: DOI: 10.1039/x0xx00000x

Yang Li, Xueliang Pei, Bin Shen, Wentao Zhai,* Lihua Zhang, and Wenge Zheng*

Received 00th January 2012,

Accepted 00th January 2012

DOI: 10.1039/x0xx00000x

www.rsc.org/

Herein Kapton-type aromatic polyimide (PI) composite foams with reduced graphene oxide (rGO) content arranging from 1 to 16 wt. % have been fabricated via a three-step method: in situ polymerization, nonsolvent induced phase separation and thermal imidization, and used for electromagnetic interference shielding. The resultant PI/16 wt. % rGO foam with low density of 0.28 g/cm³ and thickness of 0.8 mm exhibited an effective EMI shielding effectiveness of 17–21 dB in X band (8–12 GHz). Additionally, the thermostability of the foams was also significantly enhanced, for the 5% weight loss temperature was improved from 508 °C for the pure PI foam to 520 °C for the PI/1 wt. % rGO foam, and consequently, to 581 °C for the PI/16 wt. % rGO foam. Even with the high rGO content (16 wt. %), the composite foam was fairly flexible. Tensile testing revealed that the PI/16 wt. % rGO foam possessed a tensile strength of 11.4 MPa and an elongation at break of 9.6%, respectively.

1 INTRODUCTION

Nowadays, portable electronics, such as smartphone, netbook and table PCs, are being developed at a tremendous speed, leading to a high level of electromagnetic radiation pollution in our surrounding environment. Too much electromagnetic radiation represents a serious hazard to the normal working of electronic devices that are associated with strategic systems, such as aircraft, nuclear reactors, transformers, control systems and communication systems.^{1–2} Therefore, electromagnetic interference (EMI) shielding materials are required. In contrast with common metallic shields, conductive polymer composites (CPCs) possess superior properties of low density, resistance to corrosion, flexibility and excellent processibility, and have been widely investigated for EMI shielding.^{3–6} As a crucial conductive filler, graphene has drawn considerable attention in scientific community due to its high electrical conductivity, huge specific surface area as well as large aspect ratio.^{7–8} These unique properties have made it very promising in fabricating EMI shielding materials.^{9–15}

Being lightweight means a lot for practical EMI shielding systems, and foaming technique provides a good option to fulfil this target. By foaming technique, researchers may reduce the density of a shield and enhance its microwave attenuation either by improving its impedance matching with that of ambient atmosphere,¹⁶ or by promoting the multiple reflections inside

cells.^{17–18} Thomassin et al., for example, reported that the polycaprolactone (PCL) composite foam with 0.25 vol. % multi-walled carbon nanotubes (MWNTs) exhibited an EMI shielding effectiveness (SE) of 60–80 dB over the frequency range of 8–12 GHz (X band), about four times higher than that of the unfoamed counterpart.¹⁶ Ameli et al. fabricated polypropylene (PP)/stainless-steel fiber composite using foam injection molding and found that the SE of the bulk composite with stainless-steel fiber loading of 1.5 vol. % was 40.9 dB, while that of the foamed counterpart reached to 47.6 dB, about 15% increase.¹⁹ Similar phenomenon was also observed in their another report.²⁰ Moreover, the EMI shielding mechanism for most CPC foams is dominated by absorption,^{16–21} greatly reducing the risk of secondary pollution caused by the reflection of electromagnetic wave.

The typical polymer foams for EMI shielding are PP,^{19–20} polymethylmethacrylate (PMMA),²² polystyrene (PS),^{4, 23} PCL,¹⁶ polyurethane (PU),²⁴ polyvinylidene fluoride (PVDF),²⁵ and poly(dimethyl siloxane) (PDMS).²¹ Most of them are unsuitable to be employed in electronic industries, where shielding materials with high heat resistance, excellent flame retardancy, and low smoke generation are required. Therefore, our group used polyetherimide (PEI) as a matrix and fabricated high-performance polyetherimide (PEI)/graphene and PEI/graphene@Fe₃O₄ foams.^{17–18} The highest SE reached to 14–18 dB when the filler loading was 10 wt. %. Though PEI

possesses the T_g of 215 °C and the long time operating temperature of 160-180 °C, its heat resistance performance may not be sufficient to meet the harsh requirement of aeronautics and aerospace industries. In addition, with modern electronics getting smaller and faster, it has become a challenge to fabricate EMI shields with low thickness, high thermostability as well as effective SE.

Aromatic polyimide (PI) possesses high thermal stability (> 500 °C), high T_g (> 250 °C), and excellent flame retardancy, which makes it very promising in aeronautics and aerospace industries.²⁶⁻²⁸ PI foam can be prepared by different foaming methods and low foam density of 8-30 kg/m³ has been reached.²⁸⁻³⁰ Recently, Liu et al. used a silver coating process to prepare PI foam for EMI shielding.³¹ Due to the high electronic conductivity of Ag, the Ag-coated PI foam exhibited a SE of 61.6-95.6 dB over the frequency range of 0.2-7.0 GHz. To the best of our knowledge, there are rarely other open reports on the usage of PI foams as EMI shields.

In this study, Kapton-type PI/reduced graphene oxide (rGO) foams have been fabricated via a three-step method and used as an EMI shield. Details were as follows. Poly (amic acid) (PAA)/rGO casting solutions were initially synthesized via *in situ* polymerization. Meanwhile, parts of PAA were grafted from the basal plane of rGO, improving their interfacial interactions. The casting solutions were then foamed via a nonsolvent induced phase separation (NIPS) method. By thermal imidization, PAA was transferred into PI and the porous structure was well preserved. The as-prepared PI/rGO foams with low density exhibited excellent thermostability, high electrical conductivity, effective EMI SE at low sample thickness and sufficient mechanical properties, fulfilling our target of fabricating a lightweight EMI shield with low thickness, high thermostability as well as effective SE.

2 Experimental

2.1 Materials

Graphite oxide was firstly synthesized using a modified Hummers method,³² from natural graphite with a mean size of 35 μm (Qingdao Huatai Lubricant Sealing S&T). The graphite oxide was then thermally exfoliated and reduced to rGO at

180 °C for 10 min, leading to a C/O atom ratio of 5.6. 4,4'-diaminodiphenyl ether (ODA), pyromellitic dianhydride (PMDA) and N,N'-dimethylformamide (DMF) were purchased from Sinopharm Chemical Reagent (China) and used as received without further purification.

2.2 Preparation of PAA/rGO casting solutions via *in situ* polymerization

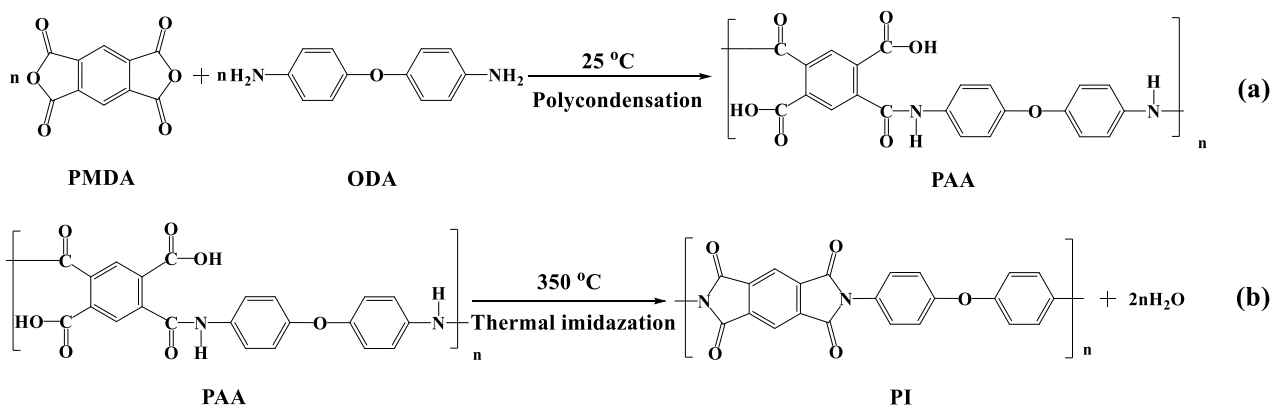
Firstly, rGO was dispersed in DMF at room temperature with the help of ultrasonication for 2 h in the presence of ODA. Then PMDA, with an equivalent molar ratio to ODA, was added. The polycondensation (Scheme 1a) occurred at room temperature for 8 h and PAA/rGO casting solution was obtained. Similarly, PAA/rGO solutions with rGO loading of 0, 1, 2, 4, 8, 12, 16 wt. % were prepared with the same method, respectively. The solid content for all was 10%.

2.3 Preparation of PAA/rGO composite foams via nonsolvent induced phase separation

To prepare PAA/rGO foams, the PAA/rGO casting solutions were firstly cast onto glass substrates and then immediately immersed into a coagulant bath composed of alcohol and distilled water with volume ratio of 1:1 at room temperature for 30 min. The as-prepared PAA/rGO composite foams were then dried in an oven at 60 °C for 12 h to remove the nonsolvent inside.

2.4 Preparation of PI/rGO composite foams via thermal imidization

PI/rGO foams were prepared from the corresponding PAA/rGO foams via thermal imidization in a controlled atmosphere furnace under nitrogen atmosphere. The PAA/rGO composite foams were heated to 100, 200 and 300 °C for 30 min each, and then at 350 °C for 1 h to guarantee the full imidization of PAA. The chemical reaction during this process has been given in Scheme 1b. The thickness of the as-obtained PI/rGO foams varies from 70 ± 5 to 100 ± 5 μm. To acquire sufficient EMI SE, another three PI/rGO foams with much higher thickness of 0.80 ± 0.01 mm were also prepared in the same way and the corresponding rGO contents were 8, 12 and 16 wt. %.



Scheme 1 Reaction schematic for polycondensation between PMDA and ODA (a) and thermal imidization of PAA (b).

2.5 Characterization

The morphology of the foams was imaged by a Hitachi TM-1000 scanning electron microscope (SEM). The samples were freeze-fractured after immersion in liquid nitrogen for 30 min, dried at 50 °C for 2 h, and then coated with platinum prior to the SEM observation. The distribution of rGO in PI matrix was examined using TECNAI 20 transmission electron microscope (TEM) at an accelerating voltage of 75 kV. The PI/rGO foams needed to be embedded in epoxy resin, cryogenically cut into ultrathin pieces with diamond knife using a microtome and collected on copper grids. XPS was performed with a Kratos AXIS ULTRA system using Al (mono) $K\alpha$ radiation. Fourier transform infrared (FT-IR) measurements were conducted on a Thermo Nicolet 6700 spectrometer. Raman spectra were collected using Labram spectrometer (Super LabRam II system) with a laser of 633 nm. Thermal gravimetric analysis (TGA) was recorded using a Mettler-Toledo TG/DSC1 analyzer (Switzerland) from 100 °C to 1000 °C at a heating rate of 20 °C/min under a nitrogen flow (20 ml/min). The volume electrical conductivity of the composite foams was examined by an EST121 ultrahigh resistance and microcurrent meter (Beijing EST Science & Technology CO. Ltd.) according to ASTM D257 when the value was lower than 1×10^{-6} S/m. Above this value (1×10^{-6} S/m), a standard four-probe method on a Napson Cresbox Measurement System was utilized to record the samples' electrical conductivity. The EMI SE was measured with a WILTRON 54169A scalar measurement system in the frequency range of 8-12 GHz at room temperature. The samples should be cut into rectangle plates with a dimension of 22.5 mm \times 10.0 mm to fit the sample holder. As mentioned above, all sample thickness sample thickness was almost the same about 0.8 mm. This value was recorded with an electronic micrometer (Shanhe Measuring Tool Co., Ltd., Chengdu). The density of the foams was calculated geometrically. Tensile properties of the samples were tested according to ASTM D882-09 on an Instron 5567 testing machine at a crosshead speed of 5 mm/min. Each specimen was cut into a rectangle sheet with a dimension of 100 mm \times 10 mm and tested at least five samples to obtain the average data.

3 Results and discussion

3.1 Synthesis of homogeneous PAA/rGO casting solutions via *in situ* polymerization

As we know, a good dispersion of graphene in common organic solvents is the prerequisite for fabricating homogeneous polymer/graphene nanocomposites via solution blending. However, the fact is that irreversible agglomeration often happens to graphene due to its hydrophobic nature. For example, in the right vial of Fig. 1a, rGO tends to precipitate at the bottom, although it has been subjected to an ultrasonication for 2 h. However, when rGO was treated with ultrasonication in the presence of ODA, no obvious precipitation was observed (Fig. 1a). After the centrifugation of the ODA-containing suspension at 8000 rpm for 30 min, a slight black but transparent solution was obtained (Fig. 1b), implying the presence of some soluble rGO. The control (Fig. 1b), however, is colorless and transparent, showing no clear evidence of rGO. All these phenomena indicated that some interactions between rGO and ODA had been formed during ultrasonication, leading to the improved dispersion of rGO in DMF. To investigate the chemical component of the soluble rGO (noted as rGO-ODA), we extracted it by filtering the black supernatant with a 220 nm polytetrafluoroethylene (PTFE) membrane and washing repeatedly the filtrated powder with excessive DMF to remove the physically absorbed ODA. The extracted powder was then dried in an oven at 60 °C for 24 h, and then examined by XPS, FT-IR and Raman spectra, respectively.

Previous studies revealed that amine groups may serve as nucleophiles and attack the carbon atoms of epoxy groups in rGO with the assistance of ultrasonication and graft onto rGO basal plane.³³⁻³⁴ Herein, XPS was used to characterize the chemical structure of rGO and rGO-ODA. In Fig. 2a, there are four characteristic peaks for the oxygen-containing groups of rGO, including 284.8 eV (C-C), 285.9 eV (C-OH), 286.9 eV (C-O-C) and 289.2 eV (-O-C=O), respectively. In the C1s XPS of rGO-ODA (Fig. 2b), the peak intensity for epoxide groups is significantly weakened and a new peak appears at 285.1 eV that corresponds to C-N bonds, indicating the occurrence of nucleophilic substitution reaction between the amine groups of ODA and the residual epoxide groups of rGO.³⁵⁻³⁶

FT-IR and Raman spectra were used as well to further examine the chemical changes in rGO. As illustrated in Fig. 2c, the FT-IR of rGO exhibits several typical peaks at 3440 cm^{-1} (O-H stretching), 2922 and 2848 cm^{-1} (C-H stretching), 1720 cm^{-1} (C=O carboxyl stretching), 1630 cm^{-1} (C=C in aromatic ring), 1385 cm^{-1} (C-OH stretching) and 1120 cm^{-1} (C-O-C in epoxide).³⁶⁻³⁷ In that of the rGO-ODA, the peak at 1120 cm^{-1} decreases significantly in intensity and a new peak appears at 1565 cm^{-1} which is attributed to the N-H stretching vibration of C-NH-C bands, suggesting the successful reaction of the amine groups with the epoxide groups.³⁶ Furthermore, the increment in the intensity of the peak at 3440 cm^{-1} and the emergence of the new peak at 802 cm^{-1} are ascribed to the N-H stretching in amine groups and C-H stretching in benzene rings of ODA,

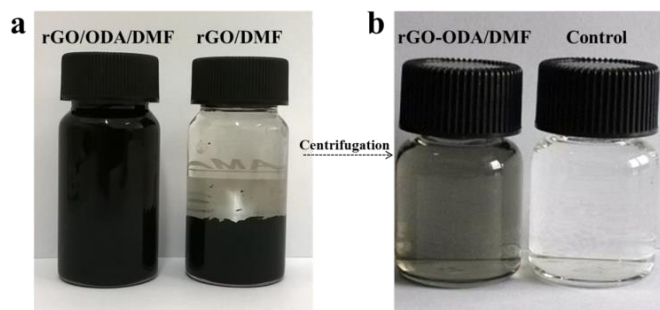


Fig. 1 Optical image of two mixtures: rGO/ODA/DMF and rGO/DMF, treated with ultrasonication at first and then stand by 1 month before taking the photos (a). Digital photo of the as-obtained supernatants after the centrifugation of the above two mixtures (b).

further demonstrating the successful grafting of ODA onto rGO basal plane. In addition, the Raman spectra of rGO and rGO-ODA were given in Fig. 2d, from which strong Raman intensities were observed within the D-band and G-band domains. In comparison with rGO, the G-band of rGO-ODA blue shifts from 1584 cm^{-1} for the rGO to 1589 cm^{-1} and the

corresponding I_D/I_G ratio increases marginally from 1.09 to 1.14. These phenomena indicate that the ordered structure of rGO has been disrupted during ultrasonication.³⁸⁻⁴⁰ The reason may be ascribed to the introduction of ODA,⁴¹ and the further exfoliation and fracture of rGO due to the cavitation effect of ultrasonication.^{38, 42}

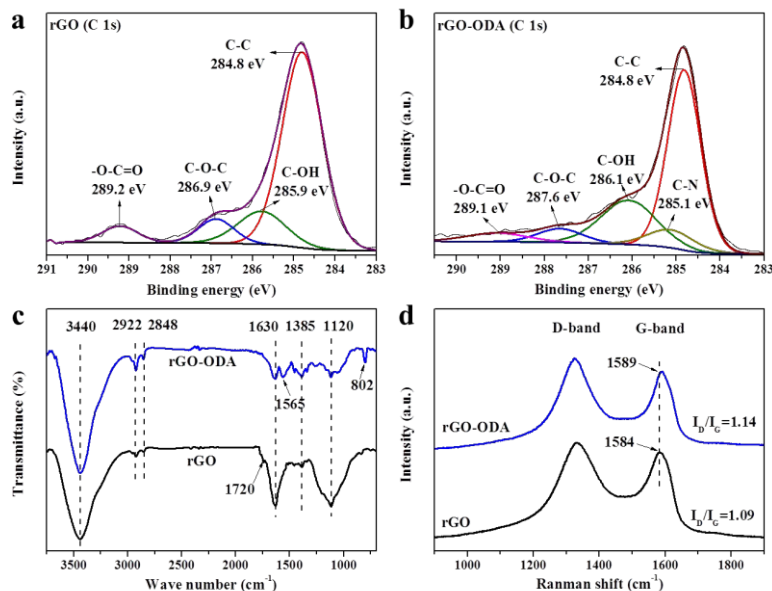
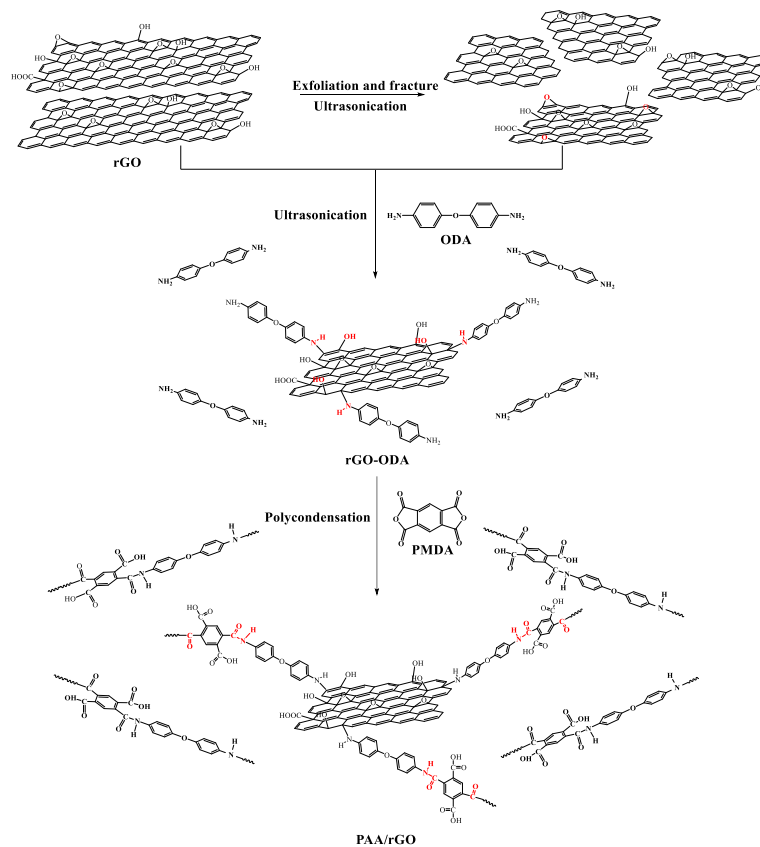


Fig. 2 C 1s XPS spectra of pristine rGO (a) and rGO-ODA (b), FT-IR spectra of pristine rGO and rGO-ODA (c), and Raman spectra of rGO and rGO-ODA (d).



Scheme 2. Schematic illustration for preparation of PAA/rGO casting solutions via *in situ* polymerization.

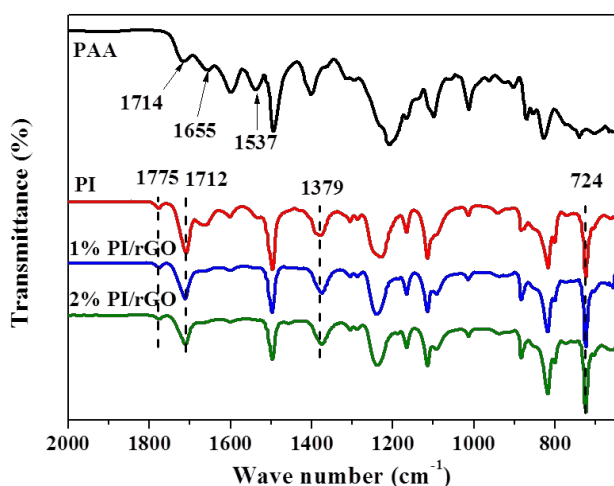


Fig. 3 FT-IR spectra of PAA, PI and PI/rGO foams.

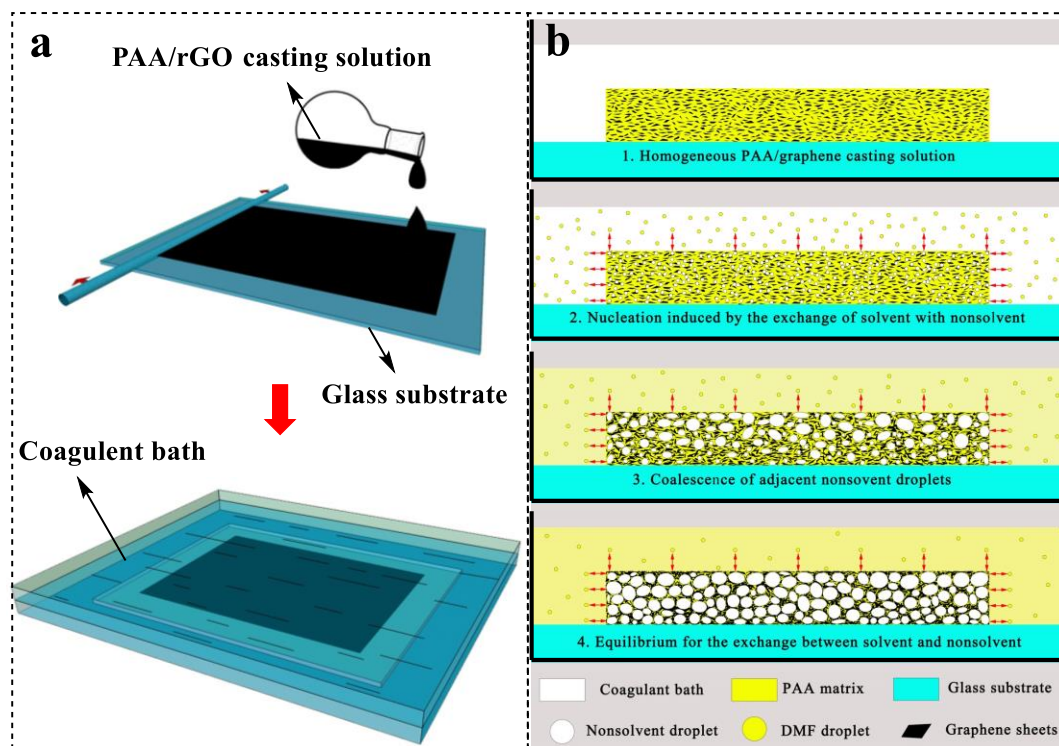
After piecing all the information together, a mechanism was proposed for the synthesis of PAA/rGO casting solution (Scheme 2). At the initial stage of the process, parts of the ODA was grafted onto the rGO basal plane via the nucleophilic substitution reaction between the amine groups of ODA and the epoxy groups of rGO with the assistance of ultrasonication, which was accompanied by further exfoliation and fracture of rGO. Once PMDA was added, the polycondensation of PAA was initiated immediately. During this process, one part of the PMDA reacted with some freedom ODA that was not grafted onto rGO, while the other part of the PMDA reacted with the terminal amine groups of the grafted ODA. As a result, parts of

PAA were grafted from rGO and homogeneous PAA/rGO casting solutions were obtained.

3.2 Preparation of PI/rGO composite foams

Prior to the preparation of PI/rGO foams, PAA/rGO foams were prepared as precursors. The fabrication of PAA/rGO foams was performed via NIPS as shown in Scheme 3a. PAA/rGO casting solution was firstly cast onto a glass substrate and then immediately immersed in a coagulant bath, inducing the occurrence of the NIPS. Generally, the phase separation process associated with NIPS consists of nucleation and growth.⁴³⁻⁴⁴ In the light of this statement, our NIPS process is composed mainly of two stages (Scheme 3b): (1) nucleation induced by the exchange of solvent with nonsolvent and (2) coalescence of adjacent cells containing nonsolvent droplets. This process is ended with the ultimate equilibrium between the exchange of solvent with nonsolvent, and PAA/rGO composite foams were achieved by removing the nonsolvent inside. The as-obtained PAA/rGO composite foams were converted into PI/rGO foams via thermal imidization at 350 °C.

To confirm the successful conversion of PI, the FT-IR of PAA, PI and PI/rGO foams were examined and the results were shown in Fig. 3. For PAA, there are three peaks at 1714, 1655 and 1537 cm^{-1} corresponding to the C=O in COOH, C=O in CONH (amide I) and C-NH stretching (amide II), respectively. In the spectra of PI and PI/rGO foams, two new peaks appear at 1775 and 1712 cm^{-1} , which are ascribed to the asymmetric and symmetric C=O stretching vibration of imide band. Another two new peaks at 1379 and 724 cm^{-1} are due to the C-N stretching and C=O bending modes of the imide groups,⁴⁵ indicating the successful conversion of PAA into PI.



Scheme 3 Schematic for NIPS operation (a) and the formation of PAA/rGO composite foams via the NIPS (b).

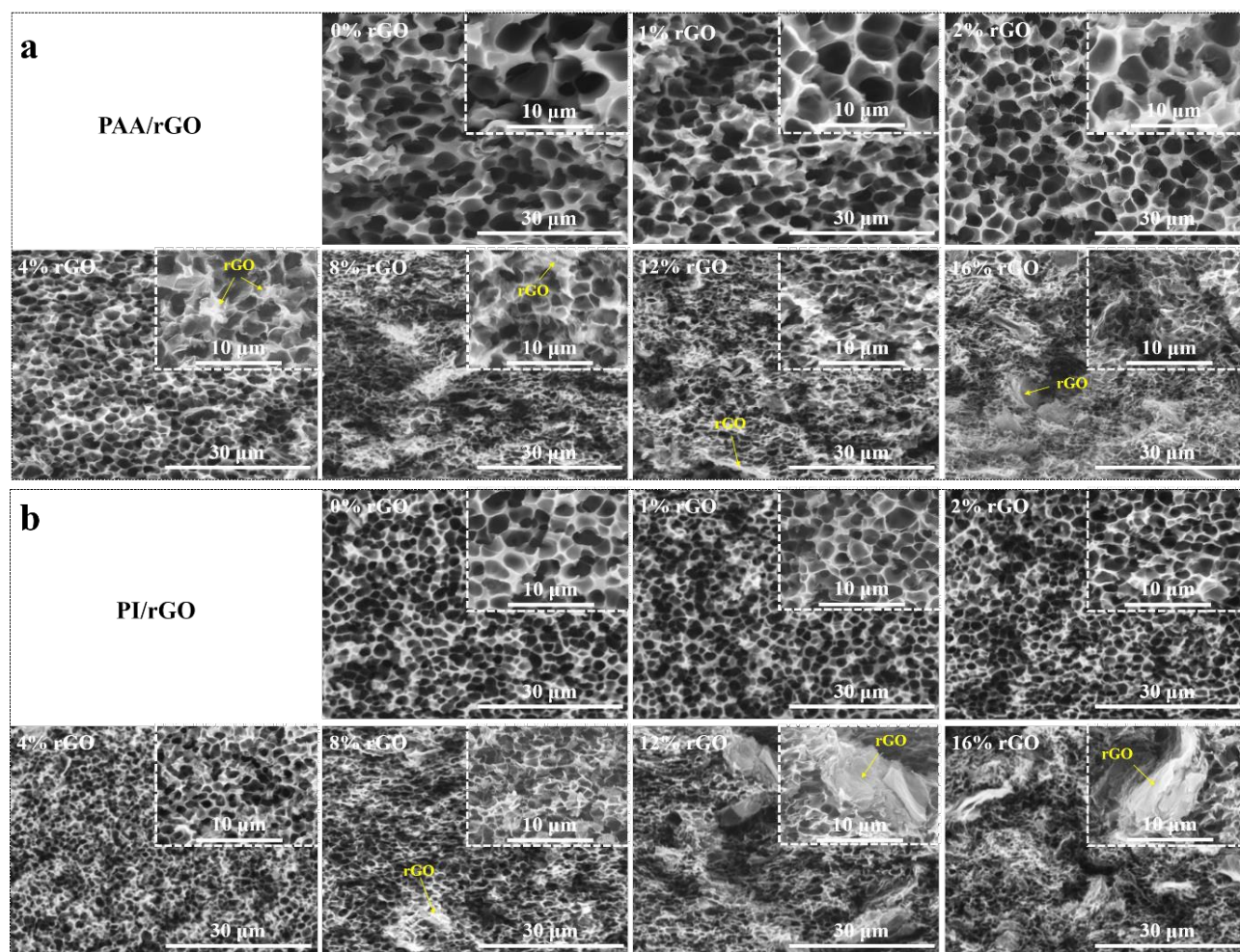


Fig. 4 Typical SEM images for PAA/rGO (a) and PI/rGO (b) composite foams with different rGO loading. The dispersion of rGO was marked with yellow arrows in parts of the pictures.

SEM was used to observe the cell morphology of PAA/rGO and PI/rGO foams and the results were shown in Fig. 4a and b, respectively. In Fig. 4a, the structure of PAA/rGO composite foams is well-defined when rGO loading is less than 8 wt. %. With further increasing rGO loading, the uniform cell structure may be disrupted by the agglomeration of rGO. The average cell size of the PAA/rGO foams in Table 1 shows a decrease tendency from $4.0 \pm 0.2 \mu\text{m}$ for pristine PAA foam to $0.8 \pm 0.1 \mu\text{m}$ for the PAA/16 wt. % rGO foam. The reason can be ascribed to the 2-fold role of rGO during the nucleation process. On one hand, rGO sheets may serve as nucleating agents, providing numerous nucleation sites for the NIPS process. On the other hand, the presence of rGO increases the viscosity of PAA/rGO casting solutions, causing physical barrier to the cell coalescence. This is a general observation for the polymer based composite foams.¹⁶⁻¹⁷ After imidization, the porous structure of PAA/rGO foams (Fig. 4b) is preserved except for some decrease in the cell size (Table 1). Furthermore, when rGO content is up to 16 wt. %, the difference in the cell size of PAA/rGO and PI/rGO foams shows a gradual decrease from 2.1 to 1.8, 1.2, 0.5, 0.4 and $0.2 \mu\text{m}$ (Table 1), suggesting that the introduction of rGO into PAA matrix helps to inhibit the

shrinkage of PAA. Generally, the more the rGO content, the more obvious the inhibited effect. The reason may be assigned to the rigid structure of rGO and the strong interfacial adhesion. The TEM image of the PI/8 wt. % rGO foam was also employed to investigate the dispersion of rGO in PI matrix. In Fig. 5, rGO tends to concentrate in the cell walls and shows a preferential orientation along the cell walls due to the biaxial stretching from PAA matrix to rGO during the cell growth. Additionally, the deformed cell structure partially stems from the plastic deformation during the slice-cutting process.

Table 1 Average cell diameter of PAA/rGO and PI/rGO composite foams and the difference between them as a function of rGO content

rGO content (wt. %)	0	1	2	4	8	12	16
$\Phi_{\text{PAA}} (\mu\text{m})$	4.0 ± 0.2	3.6 ± 0.2	2.9 ± 0.1	1.7 ± 0.1	1.4 ± 0.2	1.0 ± 0.1	0.8 ± 0.1
$\Phi_{\text{PI}} (\mu\text{m})$	1.9 ± 0.4	1.8 ± 0.2	1.7 ± 0.1	1.2 ± 0.1	1.0 ± 0.1	0.8 ± 0.1	0.6 ± 0.1
$\Phi = \Phi_{\text{PAA}} - \Phi_{\text{PI}} (\mu\text{m})$	2.1	1.8	1.2	0.5	0.4	0.2	0.2

Φ_{PAA} stands for the average cell size of PAA/rGO foams, Φ_{PI} represents the average cell size of PI/rGO foams.

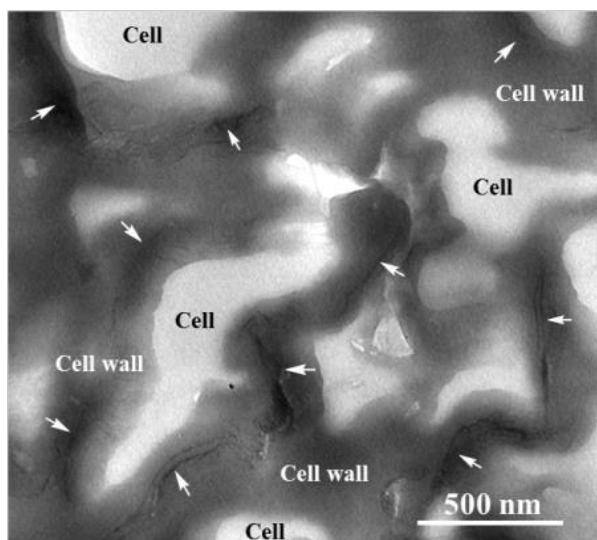


Fig. 5 TEM image of the PI/rGO foam with 8 wt. % rGO.

Table 2 shows the density of PAA/rGO and PI/rGO foams. In contrary to conventional foams,¹⁸ the density of our PAA/rGO foams exhibits a decreasing tendency with rGO content increasing. This phenomenon may be explained as follows. In the NIPS process, severe shrinkage was observed in the thickness of PAA/rGO casting solutions due to the precipitation of PAA from DMF. The existence of rGO blocks the movement of PAA chains and suppresses this shrinkage. For example, the thickness for all casting solutions is 290 μm . With the addition of rGO, the foam thickness increases gradually from $80 \pm 5 \mu\text{m}$ for pure PAA foam to $110 \pm 4 \mu\text{m}$ for PI/16 wt. % rGO. Because the weight of all PAA/rGO foams in per square centimetre is identical and the unit volume of the PAA/rGO foams increases upon rGO content. There is no doubt that the foam density decreases with rGO loading. After imidization, the density of PI/rGO foams further reduced because of the water losing in PAA macromolecules.

3.4 Thermal stability

As a high-performance plastic, thermal stability of PI is a key parameter in applications of high-tech fields. The TGA curves of PI/rGO foams, as well as the corresponding 5% weight loss temperature, are shown in Fig. 6a and b. Fig. 6b reveals that the thermal stability of PI/rGO foams is dependent on rGO loading, showing a drastically increase with increasing rGO loading. For example, the 5% weight loss temperature for the pure PI foam is 508 $^{\circ}\text{C}$, while the value increases to 520 $^{\circ}\text{C}$ with the addition of 1 wt. % rGO. Further increasing the rGO loading to 16 wt. %, the temperature was improved to 581 $^{\circ}\text{C}$. It has been said that the degradation of a polymer starts from chain cleavage and radical formation. The carbonaceous surface of rGO may act as a radical scavenger and help to put off the onset temperature for PI degradation, improving their thermal stability.⁴⁶ In addition, the high rGO content enhances the thermal conductivity of PI composites and facilitates their heat dissipation, partially improving the thermostability of the PI/rGO foams.⁴⁷

Table 2 Density of PAA/rGO and PI/rGO composite foams versus rGO content

rGO content (wt. %)	0	1	2	4	8	12	16
ρ_{PAA} (g/cm^3)	0.78	0.69	0.55	0.51	0.43	0.38	0.34
	± 0.07	± 0.04	± 0.08	± 0.03	± 0.04	± 0.04	± 0.01
ρ_{PI} (g/cm^3)	0.60	0.48	0.43	0.37	0.35	0.30	0.28
	± 0.05	± 0.03	± 0.03	± 0.02	± 0.02	± 0.02	± 0.02

ρ_{PAA} is the density of PAA/rGO composite foams, ρ_{PI} is the density of PI/rGO foams.

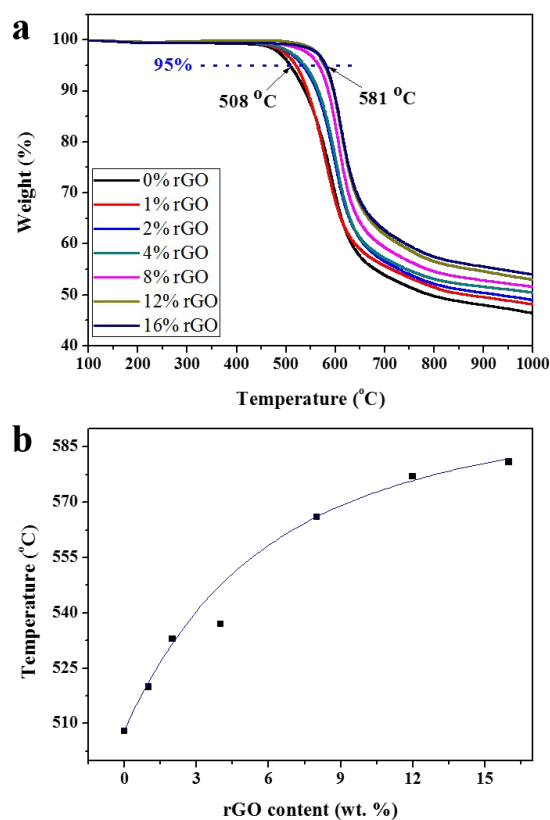


Fig. 6 TGA curves of PI/rGO foams with different rGO content (a) and relationship of 5 wt. % loss temperature with rGO content (b).

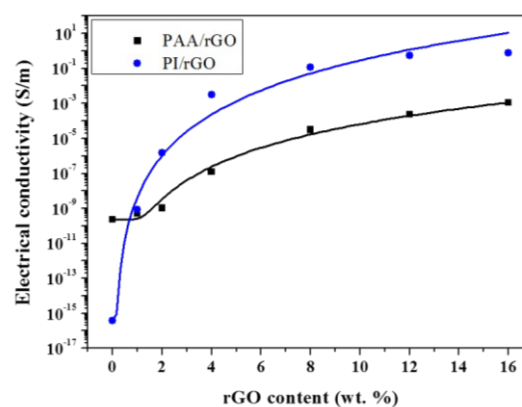


Fig. 7 Electrical conductivity of both PAA/rGO and PI/rGO composite foams versus rGO content.

3.5 Electrical conductivity

Because of the crucial role of electrical conductivity of CPCs on the EMI SE, the direct current conductivity of both PAA/rGO and PI/rGO foams was tested at first.^{4, 22, 48} In Fig. 7, the electrical conductivity increases with increasing rGO content. Both curves exhibit a dramatic increase at low rGO content, indicating the formation of conductive network within polymer matrix. For example, the electrical conductivity for pristine PI foam is 3.8×10^{-16} S/m. With the incorporation of 1 wt. % rGO, this value increases sharply to 8.2×10^{-10} S/m, which is attributed to the high aspect ratio and electrical conductivity of rGO.⁴⁹ The highest value of the PI/rGO foams reaches to 0.8 S/m when rGO loading is up to 16 wt. %. Moreover, PI foams possess much higher electrical conductivity than the PAA counterparts. The main reason is assigned to the improved reduction degree of the rGO in PI matrix. Because the rGO in PI was annealed at 350 °C for 1 h during imidization, while the thermal treatment for the rGO in PAA was just conducted at 180 °C for 10 min.

3.6 EMI shielding performance

To acquire effective EMI SE, PI/rGO foams with rGO loading of 8, 12 and 16 wt. % were selected for the EMI testing due to their high electrical conductivity. In Fig. 8a, the EMI SE of the foams is relatively frequency-independent over the X-band frequency range. With the addition of 8 wt. % rGO, the SE of the foam varies from 7.5 to 11.1 dB. The value increases to 11.7–15.3 dB when rGO loading is up to 12 wt. %. The highest SE is 17.0–21.1 dB for the foam with 16 wt. % rGO, further confirming that EMI SE can be enhanced by electrical conductivity.⁴⁸ Previous reports revealed that a sufficient thickness is one of the crucial factors for a shield to acquire satisfactory EMI SE, especially for obtaining a high microwave absorption.^{12–13} Generally speaking, the higher the shielding thickness, the higher the microwave absorption. In this article, however, the thickness for our foams is only of 0.80 ± 0.01 mm, much lower than that of typical shielding materials (≥ 2.0 mm).^{17–20} The effective SE may be the synergic effect of the porous structure of the PI/rGO foams and the high rGO loading. Furthermore, it is worth noting that the highest specific EMI SE for our PI/rGO foams is 75 dB/(g/cm³), which is higher than that of PMMA/graphene foam (24 dB/(g/cm³), 2.4 mm),²² PEI/graphene@Fe₃O₄ foam (42 dB/(g/cm³), 2.5 mm),¹⁸ PEI/graphene foam (44 dB/(g/cm³), 2.3 mm),¹⁷ and PS/graphene foam (64 dB/(g/cm³), 2.5 mm),²³ and suggests a great potential in the applications of future high-performance EMI shielding materials.

With any kind of EMI waves, there are three basic mechanisms for the EMI shielding: reflection, absorption and multiple reflections.^{48, 50} The total EMI SE (SE_{total}) is the sum of absorption (SE_A), reflection (SE_R) and multiple reflections (SE_M) and can be expressed as: $SE_{total} = SE_A + SE_R + SE_M$. Moreover, the SE_M is commonly neglected as SE_{total} is larger than 15 dB. The equation can be simplified as: $SE_{total} \approx SE_A + SE_R$.¹⁴ The EMI SE for our PI/rGO foams was calculated as

other reports,^{21–22} and the results were presented in Fig. 8b. Clearly, the increasing rGO loading leads to the enhancement of SE_{total} . And SE_A contributes most to the SE_{total} . For example, the SE_{total} , SE_A , and SE_R at 9.6 GHz were 10.4, 9.9, and 0.5 dB for the foam with 8 wt. % rGO, whereas the corresponding values for the foam with 16 wt. % rGO were 20, 17.6, and 2.4 dB, respectively. The results indicate that the EMI shielding mechanism is dominated by absorption rather than reflection. Specifically, the ratio of SE_A to SE_{total} decreases gradually from 95.2% for the PI/8 wt. % rGO foam to 88.0% for the PI/16 wt. % rGO foam, suggesting the obvious decreased absorbing ability of the foams. This phenomenon may be related to the cellular structure of the PI/rGO foam as revealed in Fig. 4b, for the porous structure of PI/rGO foams may attenuate the incident electromagnetic wave via multiple reflections, convert it into heat and dissipate. The PI/12 wt. % rGO and PI/16 wt. % rGO foams possess poor foam structure compared with the PI/8 wt. % rGO foam, which weakens their multiple reflections. The effect of cellular structure on microwave attenuation has also been discussed in our previous reports^{18, 22}.

From the EMI shielding point of view, absorption contribution originates mainly from dielectric and magnetic loss.^{51–52} For rGO, it is nonmagnetic and contributes to microwave absorption mainly through dielectric loss.^{49, 53} The interfaces between rGO and PI matrix can also induce interfacial polarization and the associated relaxation (called the Maxwell-Wagner effect) and contribute to the dielectric loss.⁵⁴ The dielectric loss is also influenced by the structure of shields,⁵⁵ for the porous structure of PI/rGO foams may help to attenuate incident electromagnetic waves via the multiple reflections. In addition, the residual oxygen groups and defects in rGO may partially contribute the microwave absorption.¹⁸

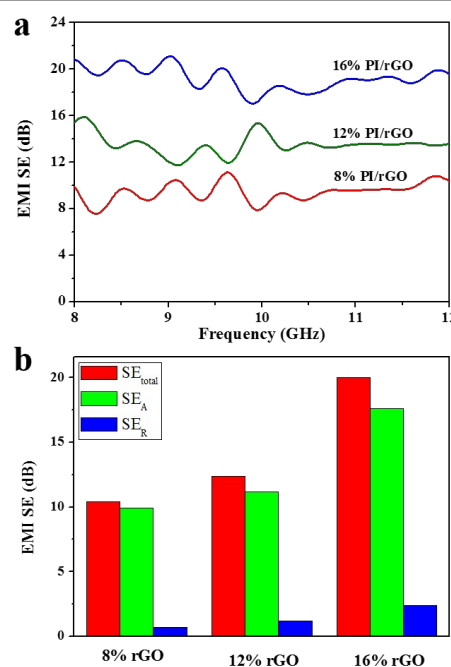


Fig. 8 EMI SE of PI/rGO foams with different rGO content in X band (a) and the corresponding SE_{total} , SE_A and SE_R at 9.6 GHz (b).

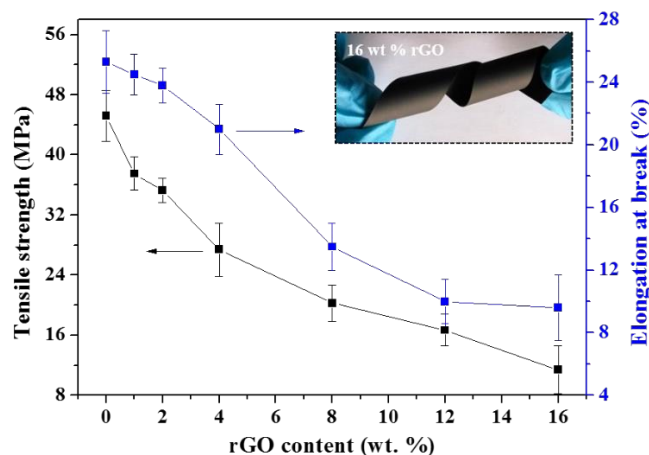


Fig. 9 Tensile properties of PI/rGO foams as a function of rGO content. The inset is the PI foam containing 16 wt. % rGO.

3.7 Mechanical properties

Generally, CPCs at high filler loading trend to become brittle.⁴ However, in the inset of Fig. 9, our PI/rGO foam with a high rGO loading of 16 wt. % is fairly flexible. To better understanding the mechanical properties of PI/rGO foams, tensile testing was conducted and the results were shown in Fig. 9. It is clear that PI/rGO foams exhibit a decreasing tendency with rGO content in both the tensile strength and the elongation at break. For example, the pristine PI foam has a tensile strength of 1034.4 MPa and an elongation at break of 25.3%. These values decrease gradually to 11.4 MPa and 9.6% with rGO content up to 16 wt. %. The decrement in the elongation at break can be assigned to the strong interfacial interactions between rGO and PI matrix, which reduces the flexibility of the foams to some extent. As to the decrease in the tensile strength, it may be ascribed to the overloaded rGO in PI matrix. Zhang et al. reported that there was an optimum functionalized graphene (FGS) concentration about 0.75 wt. % for the enhancement of PI nanocomposites.⁵⁶ In the current study, the rGO concentration in PI matrix is as high as 16 wt. %, which may exert a negative impact on the synthesis of PAA, and consequently, the tensile strength of PI/rGO foams. Nevertheless, the tensile strength of 11.4 MPa is much higher than the 3.5 MPa for our previous PEI/graphene foam with 7 wt. % graphene,¹⁷ and sufficient for many practical applications.

4 Conclusion

In this study, PI composite foams with rGO content arranging from 1 to 16 wt. % were fabricated via a three-step method: *in situ* polymerization, NIPS and thermal imidization. Meanwhile, chemical binding was formed between rGO and PI matrix. The PI composite foam with 16 wt. % rGO exhibited an excellent EMI SE of 17-21 dB in X band when the sample thickness was only of 0.8 mm. The corresponding specific EMI SE was 75 dB cm³ g⁻¹ and absorption was proved to be the dominant EMI shielding mechanism. Additionally, the thermostability of PI/rGO foams was significantly enhanced by rGO. The 5% weight loss temperature reached to 581 °C for the foam with 16

wt. % rGO. Even with the high rGO loading (16 wt. %), the resultant PI foam was fairly flexible. This technique offers a good option to manufacture high-performance EMI shielding materials with light weight, low thickness as well as high thermostability for applications in aerospace and electronic industries.

Acknowledgements

This work was financially supported by National Natural Science Foundation of China (Grant No. 51473181), National High Technology Research and Development Program ("863" Program) of China (Grant No. 2013AA032003) and Natural Science Foundation of Ningbo City, China (Grant No. 2014A610139).

Notes and references

Ningbo Key Lab of Polymer Materials, Ningbo Institute of Material Technology and Engineering, Chinese Academy of Sciences, Ningbo, Zhejiang province, 315201, China. E-mail: wzжай@nimte.ac.cn; wgzһeng@nimte.ac.cn.

- B. Shen, W. Zhai and W. Zheng, *Adv. Funct. Mater.*, 2014, **24**, 4542-4548.
- D. D. L. Chung, *Carbon*, 2012, **50**, 3342-3353.
- N. Li, Y. Huang, F. Du, X. B. He, X. Lin, H. J. Gao, Y. F. Ma, F. F. Li, Y. S. Chen and P. C. Eklund, *Nano Lett.*, 2006, **6**, 1141-1145.
- Y. Yang, M. C. Gupta, K. L. Dudley and R. W. Lawrence, *Nano Lett.*, 2005, **5**, 2131-2134.
- W. Zhai, Y. Chen, J. Ling, B. Wen and Y.-W. Kim, *J. Cell. Plast.*, 2014, **50**, 537-550.
- R. Rohini and S. Bose, *ACS Appl. Mater. Interfaces*, 2014, **6**, 11302-11310.
- K. S. Novoselov, A. K. Geim, S. V. Morozov, D. Jiang, Y. Zhang, S. V. Dubonos, I. V. Grigorieva and A. A. Firsov, *Science*, 2004, **306**, 666-669.
- S. Park and R. S. Ruoff, *Nat Nanotechnol.*, 2009, **4**, 217-224.
- S. T. Hsiao, C. C. M. Ma, H. W. Tien, W. H. Liao, Y. S. Wang, S. M. Li and Y. C. Huang, *Carbon*, 2013, **60**, 57-66.
- B. Yuan, C. Bao, X. Qian, L. Song, Q. Tai, K. M. Liew and Y. Hu, *Carbon*, 2014.
- A. P. Singh, P. Garg, F. Alam, K. Singh, R. B. Mathur, R. P. Tandon, A. Chandra and S. K. Dhawan, *Carbon*, 2012, **50**, 3868-3875.
- W. L. Song, M. S. Cao, M. M. Lu, S. Bi, C. Y. Wang, J. Liu, J. Yuan and L. Z. Fan, *Carbon*, 2014, **66**, 67-76.
- K. Singh, A. Ohlan, V. H. Pham, R. Balasubramaniyan, S. Varshney, J. Jang, S. H. Hur, W. M. Choi, M. Kumar, S. K. Dhawan, B. S. Kong and J. S. Chung, *Nanoscale*, 2013, **5**, 2411-2420.
- S. Maiti, N. K. Shrivastava, S. Suin and B. B. Khatua, *ACS Appl. Mater. Interfaces*, 2013, **5**, 4712-4724.
- H. B. Zhang, W. G. Zheng, Q. Yan, Z. G. Jiang and Z. Z. Yu, *Carbon*, 2012, **50**, 5117-5125.
- J.-M. Thomassin, C. Pagnouille, L. Bednarz, I. Huynen, R. Jerome and C. Detrembleur, *J. Mater. Chem.*, 2008, **18**, 792-796.
- J. Q. Ling, W. T. Zhai, W. W. Feng, B. Shen, J. F. Zhang and W. G. Zheng, *ACS Appl. Mater. Interfaces*, 2013, **5**, 2677-2684.
- B. Shen, W. T. Zhai, M. M. Tao, J. Q. Ling and W. G. Zheng, *ACS Appl. Mater. Interfaces*, 2013, **5**, 11383-11391.

19. A. Ameli, M. Nofar, S. Wang and C. B. Park, *ACS Appl. Mater. Interfaces*, 2014, **6**, 11091-11100.
20. A. Ameli, P. U. Jung and C. B. Park, *Carbon*, 2013, **60**, 379-391.
21. Z. P. Chen, C. Xu, C. Q. Ma, W. C. Ren and H. M. Cheng, *Adv. Mater.*, 2013, **25**, 1296-1300.
22. H. B. Zhang, Q. Yan, W. G. Zheng, Z. X. He and Z. Z. Yu, *ACS Appl. Mater. Interfaces*, 2011, **3**, 918-924.
23. D. X. Yan, P. G. Ren, H. Pang, Q. Fu, M. B. Yang and Z. M. Li, *J. Mater. Chem.*, 2012, **22**, 18772-18774.
24. M. Mar Bernal, I. Molenberg, S. Estravis, M. Angel Rodriguez-Perez, I. Huynen, M. Angel Lopez-Manchado and R. Verdejo, *J. Mater. Sci.*, 2012, **47**, 5673-5679.
25. V. Eswarajah, V. Sankaranarayanan and S. Ramaprabhu, *Macromol. Mater. Eng.*, 2011, **296**, 894-898.
26. M. Inagaki, N. Ohta and Y. Hishiyama, *Carbon*, 2013, **61**, 1-21.
27. M. Yoonessi, Y. Shi, D. A. Scheiman, M. Lebron-Colon, D. M. Tigelaar, R. A. Weiss and M. A. Meador, *Acs Nano*, 2012, **6**, 7644-7655.
28. B. Krause, G. H. Koops, N. F. A. van der Vegt, M. Wessling, M. Wubbenhorst and J. van Turnhout, *Adv. Mater.*, 2002, **14**, 1041-1046.
29. X.-Y. Liu, M.-S. Zhan, K. Wang, Y. Li and Y.-F. Bai, *Polym. Advan. Technol.*, 2012, **23**, 677-685.
30. M. K. Williams, D. B. Holland, O. Melendez, E. S. Weiser, J. R. Brenner and G. L. Nelson, *Polym. Degrad. Stabil.*, 2005, **88**, 20-27.
31. X.-Y. Liu, M.-S. Zhan and K. Wang, *J. Appl. Polym. Sci.*, 2013, **127**, 4129-4137.
32. W. S. Hummers and R. E. Offeman, *J. Am. Chem. Soc.*, 1958, **80**, 1339-1339.
33. Z. Lin, Y. Liu and C. P. Wong, *Langmuir*, 2010, **26**, 16110-16114.
34. S. Park, D. A. Dikin, S. T. Nguyen and R. S. Ruoff, *J. Phys. Chem. C*, 2009, **113**, 15801-15804.
35. J. Dong, C. Yin, X. Zhao, Y. Li and Q. Zhang, *Polymer*, 2013, **54**, 6415-6424.
36. W. Li, X.-Z. Tang, H.-B. Zhang, Z.-G. Jiang, Z.-Z. Yu, X.-S. Du and Y.-W. Mai, *Carbon*, 2011, **49**, 4724-4730.
37. W.-H. Liao, S.-Y. Yang, J.-Y. Wang, H.-W. Tien, S.-T. Hsiao, Y.-S. Wang, S.-M. Li, C.-C. M. Ma and Y.-F. Wu, *ACS Appl. Mater. Interfaces*, 2013, **5**, 869-877.
38. G.-Q. Qi, J. Cao, R.-Y. Bao, Z.-Y. Liu, W. Yang, B.-H. Xie and M.-B. Yang, *J. Mater. Chem. A*, 2013, **1**, 3163-3170.
39. H.-B. Zhang, J.-W. Wang, Q. Yan, W.-G. Zheng, C. Chen and Z.-Z. Yu, *J. Mater. Chem.*, 2011, **21**, 5392-5397.
40. B. Shen, D. D. Lu, W. T. Zhai and W. G. Zheng, *J. Mater. Chem. C*, 2013, **1**, 50-53.
41. O.-K. Park, J.-Y. Hwang, M. Goh, J. H. Lee, B.-C. Ku and N.-H. You, *Macromolecules*, 2013, **46**, 3505-3511.
42. C. Hou, Q. Zhang, Y. Li and H. Wang, *Carbon*, 2012, **50**, 1959-1965.
43. D.-M. Wang and J.-Y. Lai, *Curr. Opin. Chem. Eng.*, 2013, **2**, 229-237.
44. H. C. Park, Y. P. Kim, H. Y. Kim and Y. S. Kang, *J. Membrane Sci.*, 1999, **156**, 169-178.
45. L. Nguyen Dang, U. Hippel, J. T. Korhonen, A. J. Soininen, J. Ruokolainen, L.-S. Johansson, J.-D. Nam, L. H. Sinh and J. Seppala, *Polymer*, 2011, **52**, 5237-5242.
46. H. W. Ha, A. Choudhury, T. Kamal, D.-H. Kim and S.-Y. Park, *ACS Appl. Mater. Interfaces*, 2012, **4**, 4623-4630.
47. T. Huang, Y. Xin, T. Li, S. Nutt, C. Su, H. Chen, P. Liu and Z. Lai, *ACS Appl. Mater. Interfaces*, 2013, **5**, 4878-4891.
48. D. D. L. Chung, *Carbon*, 2001, **39**, 279-285.
49. J. J. Liang, Y. Wang, Y. Huang, Y. F. Ma, Z. F. Liu, F. M. Cai, C. D. Zhang, H. J. Gao and Y. S. Chen, *Carbon*, 2009, **47**, 922-925.
50. C. X. Tong, *Advanced materials and design for electromagnetic interference shielding*, CRC Press, Boca Raton, FL, 2009.
51. T. Chen, F. Deng, J. Zhu, C. Chen, G. Sun, S. Ma and X. Yang, *J. Mater. Chem.*, 2012, **22**, 15190-15197.
52. C. Hu, Z. Mou, G. Lu, N. Chen, Z. Dong, M. Hu and L. Qu, *Phys. Chem. Chem. Phys.*, 2013, **15**, 13038-13043.
53. W. L. Song, M. S. Cao, M. M. Lu, J. Liu, J. Yuan and L. Z. Fan, *J. Mater. Chem. C*, 2013, **1**, 1846-1854.
54. D. Chen, G.-S. Wang, S. He, J. Liu, L. Guo and M.-S. Cao, *J. Mater. Chem. A*, 2013, **1**, 5996-6003.
55. T. K. Gupta, B. P. Singh, V. N. Singh, S. Teotia, A. P. Singh, I. Elizabeth, S. R. Dhakate, S. K. Dhawan and R. B. Mathur, *J. Mater. Chem. A*, 2014, **2**, 4256-4263.
56. L.-B. Zhang, J.-Q. Wang, H.-G. Wang, Y. Xu, Z.-F. Wang, Z.-P. Li, Y.-J. Mi and S.-R. Yang, *Compos. Part A-Appl. S.*, 2012, **43**, 1537-1545.